HHS Public Access

Author manuscript

Neuroimage. Author manuscript; available in PMC 2018 February 15.

Published in final edited form as:

Neuroimage. 2017 February 15; 147: 800–811. doi:10.1016/j.neuroimage.2016.09.064.

Rapid Simultaneous High-resolution Mapping of Myelin Water Fraction and Relaxation Times in Human Brain using BMC-mcDESPOT

Mustapha Bouhrara[*] and **Richard G. Spencer**[*]

Magnetic Resonance Imaging and Spectroscopy Section, Laboratory of Clinical Investigation, National Institute on Aging, National Institutes of Health, Baltimore, MD 21224, USA

Abstract

A number of central nervous system (CNS) diseases exhibit changes in myelin content and magnetic resonance longitudinal, T_1, and transverse, T_2, relaxation times, which therefore represent important biomarkers of CNS pathology. Among the methods applied for measurement of myelin water fraction (MWF) and relaxation times, the multicomponent driven equilibrium single pulse observation of T_1 and T_2 (mcDESPOT) approach is of particular interest. mcDESPOT permits whole brain mapping of multicomponent T_1 and T_2, with data acquisition accomplished within a clinically realistic acquisition time. Unfortunately, previous studies have indicated the limited performance of mcDESPOT in the setting of the modest signal-to-noise range of high-resolution mapping, required for the depiction of small structures and to reduce partial volume effects. Recently, we showed that a new Bayesian Monte Carlo (BMC) analysis substantially improved determination of MWF from mcDESPOT imaging data. However, our previous study was limited in that it did not discuss determination of relaxation times. Here, we extend the BMC analysis to the simultaneous determination of whole-brain MWF and relaxation times using the two-component mcDESPOT signal model. Simulation analyses and *in-vivo* human brain studies indicate the overall greater performance of this approach compared to the stochastic region contraction (SRC) algorithm, conventionally used to derive parameter estimates from mcDESPOT data. SRC estimates of the transverse relaxation time of the long T_2 fraction, $T_{2,l}$, and the longitudinal relaxation time of the short T_1 fraction, $T_{1,s}$, clustered towards the lower and upper parameter search space limits, respectively, indicating failure of the fitting procedure. We demonstrate that this effect is absent in the BMC analysis. Our results also showed improved parameter estimation for BMC as compared to SRC for high-resolution mapping. Overall we find that the combination of BMC analysis and mcDESPOT, BMC-mcDESPOT, shows excellent performance for accurate high-resolution whole-brain mapping of MWF and bi-component transverse and longitudinal relaxation times within a clinically realistic acquisition time.

[*]Corresponding author. Mustapha Bouhrara, Ph.D. NIH/National Institute on Aging, Intramural Research Program, BRC 04C-001, 251 Bayview Boulevard, Baltimore, MD 21224, USA. Tel: 410-558-8541. [*]Corresponding author. Richard G. Spencer, M.D., Ph.D. NIH/National Institute on Aging, Intramural Research Program, BRC 04B-116, 251 Bayview Boulevard, Baltimore, MD 21224, USA. Tel: 410-558-8226.

Keywords

Brain; MRI; High-resolution mapping; Myelin water fraction; Relaxation times

1. INTRODUCTION

Alterations in myelin content and in magnetic resonance relaxation times T_1 and T_2 have been shown to be sensitive biomarkers for a number of central nervous system diseases. These include multiple sclerosis (1–5), brain atrophy (6, 7), epilepsy (8–11), Parkinson's disease (7), Alzheimer's disease (12, 13), phenylketonuria (14, 15), psychotic disorders (16), and schizophrenia (17–20). While it is most often assumed that relaxation within each imaging voxel may be described by a single T_1 or T_2 value, this assumption does not capture the structural and compositional complexity of brain tissue. In fact, previous studies have demonstrated the presence of multi-component T_1 and T_2 relaxation processes in brain as an indicator of compartmentation (5, 21–33). Multicomponent relaxometry (MCR) analysis has characterized two main water pools, with distinct relaxation times and fractions. The pool exhibiting the more rapid transverse relaxation and smaller fraction size has been attributed to myelin-bound water, while the more slowly-relaxing pool has been assigned to relatively unbound intra- and extracellular water (21, 23, 28, 34).

A variety of approaches to MCR have been applied to *in-vivo* clinical studies (28, 29, 32, 35–43), and have been reviewed recently by Alonso-Ortiz *et al.* (23). Among these methods, the multicomponent driven equilibrium single pulse observation of T_1 and T_2 (mcDESPOT) method, based on steady-state magnetic resonance imaging (MRI) sequences, is of particular interest (28, 44). mcDESPOT allows simultaneous mapping of multicomponent T_1 and T_2 relaxation times and myelin water fraction (MWF), providing improved sensitivity and specificity to tissue changes associated with development or pathology. Moreover, mcDESPOT permits the use of a relatively short echo time, TE, thereby allowing improved detection of the short-T_2 component of the signal, representing the MWF. Finally, mcDESPOT makes use of conventional MR acquisition sequences, namely, fully balanced steady state free precession (bSSFP) and spoiled gradient recalled echo (SPGR), widely available on clinical MRI systems. Overall, then, mcDESPOT is particularly attractive for clinical investigations (26, 30, 45).

In mcDESPOT analysis, SPGR and bSSFP datasets are acquired over a range of flip angles (FAs), with very short repetition times, TRs. Two different bSSFP datasets are acquired respectively with radio-frequency (RF) phase increments equal to 0 or π ($bSSFP_0$ and $bSSFP_\pi$) to correct for off-resonance effects (44). Although this formalism has been extended to include a third pool to account for either partial volume effects (27) or magnetization transfer (46), mcDESPOT modeling is generally restricted to a two-pool model. Even with this restriction, quantitative parameter estimation from mcDESPOT is problematic, especially at the low-to-moderate signal-to-noise ratios (SNRs) typical of high-resolution imaging (25, 47, 48). In recent studies, Zhang *et al.* (33, 49), Lankford and Does (50) and Bouhrara *et al.* (47) showed that for a two-component implementation of mcDESPOT using stochastic region contraction (SRC) with nonlinear least squares (NLLS),

determination of relaxation times was problematic due to the flatness of the parameter least-squares energy surfaces. It was found, for example, that estimates of T_1 for the more rapidly relaxing component, and of T_2 for the more slowly relaxing component, showed a tendency to cluster respectively at the upper and the lower limits of the specified parameter spaces (33, 49).

In a recent study, Bouhrara and Spencer showed that the quality of MWF estimates from the two-component mcDESPOT signal model was greatly enhanced through use of a new Bayesian Monte Carlo (BMC) analysis (25). However, that work was limited to MWF analysis and did not address the important issue of relaxation time estimation. In this work we therefore extend BMC-mcDESPOT analysis to the simultaneous estimation of MWF and relaxation times over the whole brain with a voxel volume of 1 mm^3, with an acquisition time of under 15 minutes. In addition, we directly demonstrate the superior performance of BMC compared to the conventional approach using SRC.

2. MATERIALS & METHODS

2.1. Experimental Analysis

2.1.1. Data Acquisition—All experiments were performed on a 3T whole body Philips MRI system (Achieva, Best, The Netherlands) using the internal quadrature body coil for transmission and an eight-channel phased-array head coil for reception. Data were collected at low-resolution (LR) or high-resolution (HR) from four volunteers, from whom written informed consent was obtained prior to participation. All examinations were performed with approval of the local Institutional Review Board. Table 1 summarizes the experimental acquisition and reconstruction parameters of mcDESPOT imaging data for each volunteer. LR images were obtained with an acquisition voxel size of 2 mm x 2 mm x 2 mm and reconstructed to this same voxel volume of 8 mm^3 while all HR images were acquired with an acquisition voxel size of 1.5 mm x 1.5 mm x 1.5 mm and reconstructed to a voxel volume of 1 mm^3 using zero-filling to improve visual quality.

In our *in-vivo* studies, SNR was estimated as the mean signal value within a large region in SPGR images obtained over all non-zero FAs divided by the mean signal value for FA = 0^o. These SNR values were ~30 and ~50 for the HR and LR protocols (Table 1), respectively.

2.1.2 Data Analysis—We assumed a two-component non-exchanging system consisting of a short, *s,* and long, *l,* T_1 and T_2 components (25, 28, 51). Analysis was performed explicitly accounting for nonzero TE as incorporated into the TE-corrected-mcDESPOT (TEC-mcDESPOT) signal model (52). Images from each mcDESPOT dataset were analyzed on a voxel-wise basis. First, monoexponential T_1 maps were generated through a fit of the SPGR data as a function of FAs to a functional form incorporating only a single underlying component. Similarly, T_2 and off-resonance maps were then generated according to the $DESPOT_2$-FM method (53) by fitting the bSSFP datasets as a function of FAs to a single component form of the signal, using the voxel-wise T_1 value obtained as outlined above. Finally, the off-resonance map was combined with the SPGR and bSSFP datasets to simultaneously generate f_s, $T_{2,s}$, $T_{2,l}$, $T_{1,s}$, and $T_{1,l}$ maps, with f_s defining the MWF. Manual

segmentation was performed to eliminate ventricles and non-brain regions within the images, with parameter maps generated for the remaining regions of interest.

The first analysis consisted of investigating the performance of the BMC approach for generating high-resolution MWF, $T_{2,s}$, $T_{2,l}$, $T_{1,s}$, and $T_{1,l}$ maps. Analysis was performed for all LR and HR datasets described in Table 1. Details regarding the mathematical aspects of BMC-mcDESPOT analysis for simultaneous estimation of all system parameters are given in the Appendix.

In recent studies, Zhang *et al.* (33, 49) showed that determination of relaxation times from mcDESPOT using SRC (54) can be problematic. Motivated by their observations, we performed a second analysis in which we generated MWF, $T_{2,s}$, $T_{2,l}$, $T_{1,s}$, and $T_{1,l}$ maps using SRC. This analysis was performed on the LR and HR datasets acquired from Volunteer #1 (Table 1). Wide limits for the initial parameter bounds were used to avoid an over-constrained parameter space (33, 47, 51). These limits were 1 ms ≤ $T_{2,s}$ ≤ 60 ms, 60 ms ≤ $T_{2,l}$ ≤ 200 ms, 10 ms ≤ $T_{1,s}$ ≤ 650 ms, 10 ms ≤ $T_{1,l}$ ≤ 3500 ms and 0 ≤ f_s ≤ 0.45. These same limits were used in all BMC analyses as well. Histograms of parameter values were calculated from white matter (WM) voxels in several slices, with the WM regions defined using manual segmentation of T_2 maps generated using the DESPOT$_2$-FM method described above.

Finally, the mean and SD for each estimated parameter were calculated over three regions of interest (ROIs) in several slices. The first ROI (ROI #1) lay within the frontal lobes, the second ROI (ROI #2) lay within the regions surrounded by the insular cortex, internal capsule, thalamus and putamen, and the third ROI (ROI #3) enclosed all WM regions. This analysis was performed on the parameter maps obtained from HR datasets using BMC or SRC.

2.2. Simulation Analysis

Numerical simulations were used to further assess the performance of parameter determination using BMC-mcDESPOT and for comparison with those computed using SRC. The following input parameters describing acquisition were used: TR_{SPGR} = TR_{bSSFP} = 6.5 ms, TE_{SPGR} = 1 ms, α_{SPGR} = [2 4 6 8 10 12 14 16 18 20]^o, and β_{bSSFP} = [2 6 14 22 30 38 46 54 62 70]^o, with two bSSFP datasets generated with RF phase increments of 0 or π respectively. Input parameters defining the system were: f_s (*i.e.* MWF) = 0.2, $T_{2,s}$ = 15 ms, $T_{2,l}$ = 75 ms, $T_{1,s}$ = 500 ms, and $T_{1,l}$ = 1500 ms, corresponding to WM values obtained from the *in-vivo* analysis described above. Results were obtained over 1001 noise realizations and are presented as histograms. All analyses were performed at steady-state SNR of 500, defined as SNR = M_0 / σ, where M_0 represents the signal amplitude at TE = 0 ms. This steady state SNR value corresponds to an *in-vivo* SNR of ~20–30 as defined above. More extensive numerical analyses are presented in the Supplementary Material.

3. RESULTS

Figure 1 shows examples of MWF, $T_{2,s}$, $T_{2,l}$, $T_{1,s}$ and $T_{1,l}$ maps derived from brain images using BMC-mcDESPOT. HR datasets and LR datasets were acquired with isotropic voxel

volumes of 1 mm^3 and 8 mm^3 respectively. Parameter maps derived from the HR and LR datasets were similar overall, especially in the WM regions. However, as expected, the HR maps better define anatomic details and regional patterns. The LR maps showed, overall, greater dispersion in derived parameter estimates especially at interfaces between gray and white matter, likely due to partial volume effects. Moreover, in contrast to the WM regions, all $T_{2,s}$ maps showed high dispersion in the CSF and gray matter. This is a direct consequence of the very low values of MWF in these regions, which renders it impossible to assign meaningful values of $T_{2,s}$.

Figure 2 shows examples of MWF, $T_{2,s}$, $T_{2,l}$, $T_{1,s}$, and $T_{1,l}$ parameter maps derived from the HR and LR human brain images using SRC. Parameter values derived from HR or LR were again similar, especially in WM regions. However, visual inspection (Figs. 1–2) as well as histogram analysis (Fig. 3) demonstrate that the derived parameter estimates using SRC (Fig. 2–3) differed substantially from those obtained with BMC (Figs. 1 and 3), particularly for $T_{2,s}$, $T_{2,l}$ and $T_{1,s}$. In addition, unlike BMC, SRC resulted in substantial random variation in the estimation of $T_{2,s}$, and clustering of $T_{2,l}$ and $T_{1,s}$ estimates towards the lower and upper search space limits, respectively. $T_{1,l}$ and MWF maps derived from SRC and BMC showed similar regional patterns, although lower dispersion was evident in the MWF estimates derived using BMC. These results indicate the superior overall performance of BMC as compared to SRC. We also observed that the clustering of $T_{1,s}$ estimates towards the upper search space limits using SRC was reduced to some extent in the LR parameter maps as compared to the HR maps. This is likely due to the relatively higher SNR of the former.

Figure 4 shows parameter histograms of f_s (*i.e.* MWF), $T_{2,s}$, $T_{2,l}$, $T_{1,s}$, and $T_{1,l}$ obtained using Monte Carlo simulations over 1001 noise realizations. Results were obtained at an SNR value of 500 using SRC or BMC. Using SRC, $T_{2,l}$ estimates were clustered towards the lower search space limit while $T_{1,s}$ estimates were clustered towards the upper search space limit; this behavior is in good agreement with our *in-vivo* observations (Figs. 2–3). In contrast, BMC parameter estimates were preferentially distributed around the true input values and avoided search space boundaries. Further, parameter estimates using SRC showed larger bias and dispersion compared to BMC. Extensive numerical analysis further demonstrating the overall superior performance of BMC is presented in the Supplementary Material (Fig. Sup.1).

Figure 5 shows parameter means and SDs of estimates of MWF, $T_{2,s}$, $T_{2,l}$, $T_{1,s}$, and $T_{1,l}$ calculated from the three HR datasets (Table 1). For each HR dataset, results were obtained over three ROIs using BMC and SRC analyses. The results indicate good reproducibility for both analysis methods between the three subjects for all estimated parameters. However, BMC analysis was able to detect regional variation in all system parameters, while SRC showed substantial regional changes in MWF, $T_{2,s}$ and $T_{1,l}$ only. In fact, $T_{2,l}$ and $T_{1,s}$ calculated using SRC showed artifactually decreased regional variation; the averaged values calculated over the three subjects were $T_{2,l}$ = 64 ± 3.9 ms and $T_{1,s}$ = 626 ± 7.6 ms, which are very close to the lower and upper search space limits of 60 ms and 650 ms, respectively. In contrast, the averaged values of these parameters calculated using BMC, 77 ± 2.1 ms and 517 ± 13.2 ms, were well-within the search space limits. This is consistent with Figs. 2–4

and the comments above. Finally, parameter estimates of MWF, $T_{2,s}$ and $T_{1,l}$ derived using SRC showed, overall, higher SDs as compared to those derived using BMC. In fact, the average SD values over the three volunteers in the estimation of MWF, $T_{2,s}$ and $T_{1,b}$ respectively, were 0.1, 8.2 ms and 425 ms using SRC, and 0.06, 5.4 ms and 360 ms using BMC. This is in good agreement with Fig. 2, which shows substantial spatial irregularities, especially in derived MWF and $T_{2,s}$ values, as compared to the BMC results of Fig. 1.

4. DISCUSSION

In 1994, Mackay *et al*. demonstrated *in-vivo* MCR in the human brain for myelin mapping using MRI (21). Since then, MCR has become an active area of research, with several methods having been developed to either accelerate data acquisition (23, 28, 29, 32, 36, 37, 39, 40, 55) or to improve parameter determination (23, 25, 36, 44, 56–65). Among these, mcDESPOT permits rapid whole-brain coverage, and so may have particular potential for clinical investigations, especially those involving patients with limited ability to remain stationary for the lengthy duration of MRI studies. However, it has been shown (25, 33, 47, 48) that the high dimensionality of the mcDESPOT signal models renders parameter estimation problematic when the acquired images exhibit substantial noise, such as in the case of high-resolution mapping. However, we showed that the quality of derived MWF estimates is greatly enhanced using BMC analysis (25). In the present work, we generalized BMC-mcDESPOT to the simultaneous estimation of MWF and relaxation times for a two-component model; simulation analysis demonstrated that BMC allows high quality determination of all system parameters. Further, our *in-vivo* analysis showed that high-quality, high-resolution MWF and relaxation time maps may be obtained with an isotropic voxel volume of 1 mm^3 within a clinically realistic acquisition time, permitting accurate depiction of anatomical detail and regional patterns compared to LR mapping (Fig. 1).

In this study we compared the performance of the BMC-mcDESPOT analysis with that of the SRC algorithm, conventionally used for parameter estimation with mcDESPOT, for determination of MWF and relaxation times. Overall, we found greatly reduced bias and dispersion in the estimation of all system parameters using BMC (Figs. 1–5, Fig. Sup.1). We attribute this to several factors, including the implicit incorporation of noise SD and the marginalization over nuisance parameters in the BMC analysis (25). In fact, a fundamental difference between Bayesian methods and the several variants of NLLS algorithms, such as SRC, is that the posterior probabilities resulting from the former are obtained through incorporation of the entire specified ranges of nuisance parameters through marginalizations. In contrast, the evaluation of single combinations of estimated parameters required to optimize the objective function in NLLS leads to potential difficulties with local minima, especially in higher-dimensional problems such as mcDESPOT (47). A drawback to Bayesian analysis is the requirement for high dimensional integration in order to perform the marginalizations. To overcome this, we have implemented Monte Carlo sampling to perform the required integrations, although more advanced sampling strategies such as Markov chain Monte Carlo may further improve performance (66).

Our numerical and *in-vivo* analyses showed that using SRC, $T_{2,l}$ estimates were preferentially clustered close to the lower search space limit, while $T_{1,s}$ estimates were

preferentially close to the upper search space limit (Fig. 2–4, Fig. Sup.1). This is in good agreement with the observations of Zhang *et al.* (33, 49). This problem was markedly reduced using BMC, with parameter estimates distributed around mean values that were clearly separated from the search space limits. However, visual inspection of the parameter maps (Figs. 1–2) as well as more quantitative analysis (Fig. 3–5) showed higher dispersion in derived parameter estimates as compared to the literature (26, 28, 33, 44, 49, 67), especially using SRC. We attribute this to our use of relatively large parameter space bounds to avoid bias (33, 47, 51); as has previously been noted, this comes at the expense of increased dispersion (47, 51). *A priori* restriction of the allowable parameter space therefore represents a tradeoff between bias and dispersion.

In agreement with recent studies (33, 49), our results showed that MWF and relaxation parameters values derived from mcDESPOT were substantially different from those derived from a CPMG analysis. This can be attributed to the fact that MRI pulse sequences, including mcDESPOT and CPMG, are influenced to substantially different degrees by experimental and physiological effects. Therefore, received signals will deviate from their ideal models due to diffusion (68–71), exchange (33, 72, 73), off-resonance effects (74–76), magnetization transfer (49, 77–79), *J*-coupling (80–82), spin locking (83, 84), internal gradients (85, 86), and magnetization spoiling (87, 88). The importance of these effects will depend both upon the specifics of the sample or subject under investigation and on the details of the pulse sequence, including the selection of parameters such as TE, TR, FAs, RF pulse shape, and gradient durations and amplitudes (89–93).

Our HR analyses were performed on three healthy young volunteers. While BMC showed good reproducibility between these subjects for all estimated parameters (Fig. 5), larger groups of subjects would be required for statistical comparisons between groups varying by, for example, age or disease status.

In the present work, we based our analysis on SPGR and bSSFP signal models that account for nonzero TE, that is, we used the TEC-mcDESPOT signal model (52). The neglect of the transverse signal decay that occurs during TE has been recently shown to potentially introduce large biases in parameter estimates from mcDESPOT (52). Nevertheless, limitations remain in the signal modeling of mcDESPOT, which represent limitations of the present work as well as in certain literature results. First, the mcDESPOT signal models analyzed by ourselves and others neglect finite RF pulse length (94–98). Similarly, we assumed perfect spoiling of transverse magnetization before each excitation pulse in the SPGR sequence; it has been shown that there may be a degree of preservation of transverse coherence in fast SPGR sequences with concomitant deviation of the signal behavior from the idealized model (87, 88, 99). Further, we assumed a two-component signal model; it has been shown that a three-component model improves the performance of mcDESPOT analysis in regions exhibiting partial volume effects, such as boundaries between brain tissue and ventricles and meninges (27). In addition, we assumed no exchange between the two proton pools. Extension of the BMC analysis to incorporate exchange is straightforward in principle and would permit evaluation of the impact of exchange on relaxation times, as well as on the estimate of MWF. Our analysis also assumes that the effect of magnetization transfer between free water protons and macromolecules is small (49). Moreover, we

assumed a Gaussian noise distribution for our Bayesian analysis to obtain closed form expressions for marginalized joint likelihood functions (25). However, it is well-known that the noise in magnitude MR images follows a noncentral-χ distribution (100), which can be approximated by a Gaussian distribution only for relatively high SNR. Finally, as with any MRI sequence, the spatial encoding gradients of steady-state sequences modulate the degree of signal attenuation due to water diffusion (101, 102). However, water diffusion in different compartments, such as myelin sheets and intra- and extra-cellular spaces, is not incorporated into the mcDESPOT formalism. While extensive further investigation would be required to analyze all of the above effects, the present work stands to demonstrate the feasibility of high-resolution mapping of MWF and relaxation times under clinical MRI acquisition conditions.

5. CONCLUSIONS

We have demonstrated the feasibility of simultaneous HR mapping of MWF and relaxation times in white matter regions of human brain using BMC-mcDESPOT. High-resolution whole-brain maps of MWF and transverse and longitudinal bi-component relaxation times can be obtained in less than 15 min.

Supplementary Material

Refer to Web version on PubMed Central for supplementary material.

Acknowledgments

This work was supported by the Intramural Research Program of the NIH, National Institute on Aging. We thank David A. Reiter and Christopher Bergeron for assistance with data acquisition.

References

1. Neema M, Stankiewicz J, Arora A, Dandamudi VS, Batt CE, Guss ZD, et al. T1- and T2-based MRI measures of diffuse gray matter and white matter damage in patients with multiple sclerosis. Journal of neuroimaging : official journal of the American Society of Neuroimaging. 2007; 17(Suppl 1): 16s–21s. [PubMed: 17425729]
2. Manfredonia F, Ciccarelli O, Khaleeli Z, et al. Normal-appearing brain T1 relaxation time predicts disability in early primary progressive multiple sclerosis. Archives of Neurology. 2007; 64(3):411–5. [PubMed: 17353385]
3. Ropele S, Strasser-Fuchs S, Augustin M, Stollberger R, Enzinger C, Hartung HP, et al. A comparison of magnetization transfer ratio, magnetization transfer rate, and the native relaxation time of water protons related to relapsing-remitting multiple sclerosis. AJNR American Journal of Neuroradiology. 2000; 21(10):1885–91. [PubMed: 11110542]
4. Neema M, Goldberg-Zimring D, Guss ZD, Healy BC, Guttmann CR, Houtchens MK, et al. 3 T MRI relaxometry detects T2 prolongation in the cerebral normal-appearing white matter in multiple sclerosis. NeuroImage. 2009; 46(3):633–41. [PubMed: 19281850]
5. Laule C, Vavasour IM, Moore GR, Oger J, Li DK, Paty DW, et al. Water content and myelin water fraction in multiple sclerosis. A T2 relaxation study. Journal of Neurology. 2004; 251(3):284–93. [PubMed: 15015007]
6. Nakamura K, Brown RA, Araujo D, Narayanan S, Arnold DL. Correlation between brain volume change and T2 relaxation time induced by dehydration and rehydration: implications for monitoring atrophy in clinical studies. NeuroImage Clinical. 2014; 6:166–70. [PubMed: 25379428]

7. Vymazal J, Righini A, Brooks RA, Canesi M, Mariani C, Leonardi M, et al. T1 and T2 in the brain of healthy subjects, patients with Parkinson disease, and patients with multiple system atrophy: relation to iron content. Radiology. 1999; 211(2):489–95. [PubMed: 10228533]
8. Pitkanen A, Laakso M, Kalviainen R, Partanen K, Vainio P, Lehtovirta M, et al. Severity of hippocampal atrophy correlates with the prolongation of MRI T2 relaxation time in temporal lobe epilepsy but not in Alzheimer's disease. Neurology. 1996; 46(6):1724–30. [PubMed: 8649578]
9. Conlon P, Trimble MR, Rogers D, Callicott C. Magnetic resonance imaging in epilepsy: a controlled study. Epilepsy Research. 1988; 2(1):37–43. [PubMed: 3197678]
10. Townsend TN, Bernasconi N, Pike GB, Bernasconi A. Quantitative analysis of temporal lobe white matter T2 relaxation time in temporal lobe epilepsy. NeuroImage. 2004; 23(1):318–24. [PubMed: 15325379]
11. Jackson GD, Connelly A, Duncan JS, Grunewald RA, Gadian DG. Detection of hippocampal pathology in intractable partial epilepsy: increased sensitivity with quantitative magnetic resonance T2 relaxometry. Neurology. 1993; 43(9):1793–9. [PubMed: 8414034]
12. House MJ, St Pierre TG, Foster JK, Martins RN, Clarnette R. Quantitative MR imaging R2 relaxometry in elderly participants reporting memory loss. AJNR American journal of Neuroradiology. 2006; 27(2):430–9. [PubMed: 16484425]
13. Bartzokis G, Lu PH, Mintz J. Quantifying age-related myelin breakdown with MRI: novel therapeutic targets for preventing cognitive decline and Alzheimer's disease. Journal of Alzheimer's disease : JAD. 2004; 6(6 Suppl):S53–9. [PubMed: 15665415]
14. Sirrs SM, Laule C, Madler B, Brief EE, Tahir SA, Bishop C, et al. Normal-appearing white matter in patients with phenylketonuria: water content, myelin water fraction, and metabolite concentrations. Radiology. 2007; 242(1):236–43. [PubMed: 17185670]
15. Vermathen P, Robert-Tissot L, Pietz J, Lutz T, Boesch C, Kreis R. Characterization of white matter alterations in phenylketonuria by magnetic resonance relaxometry and diffusion tensor imaging. Magnetic Resonance in Medicine. 2007; 58(6):1145–56. [PubMed: 18046700]
16. Wood SJ, Cocchi L, Proffitt TM, McConchie M, Jackson GD, Takahashi T, et al. Neuroprotective effects of ethyl-eicosapentaenoic acid in first episode psychosis: a longitudinal T2 relaxometry pilot study. Psychiatry Research. 2010; 182(2):180–2. [PubMed: 20413278]
17. Supprian T, Hofmann E, Warmuth-Metz M, Franzek E, Becker T. MRI T2 relaxation times of brain regions in schizophrenic patients and control subjects. Psychiatry Research. 1997; 75(3):173–82. [PubMed: 9437774]
18. Williamson P, Pelz D, Merskey H, Morrison S, Conlon P. Correlation of negative symptoms in schizophrenia with frontal lobe parameters on magnetic resonance imaging. The British Journal of Psychiatry : the Journal of Mental Science. 1991; 159:130–4. [PubMed: 1888960]
19. Pfefferbaum A, Sullivan EV, Hedehus M, Moseley M, Lim KO. Brain gray and white matter transverse relaxation time in schizophrenia. Psychiatry Research. 1999; 91(2):93–100. [PubMed: 10515464]
20. Flynn SW, Lang DJ, Mackay AL, Goghari V, Vavasour IM, Whittall KP, et al. Abnormalities of myelination in schizophrenia detected in vivo with MRI, and post-mortem with analysis of oligodendrocyte proteins. Molecular Psychiatry. 2003; 8(9):811–20. [PubMed: 12931208]
21. MacKay A, Whittall K, Adler J, Li D, Paty D, Graeb D. In vivo visualization of myelin water in brain by magnetic resonance. Magnetic Resonance in Medicine. 1994; 31(6):673–7. [PubMed: 8057820]
22. Bakshi R, Thompson AJ, Rocca MA, Pelletier D, Dousset V, Barkhof F, et al. MRI in multiple sclerosis: current status and future prospects. The Lancet Neurology. 2008; 7(7):615–25. [PubMed: 18565455]
23. Alonso-Ortiz E, Levesque IR, Pike GB. MRI-based myelin water imaging: A technical review. Magnetic Resonance in Medicine. 2015; 73(1):70–81. [PubMed: 24604728]
24. Bouhrara M, Reiter DA, Spencer RG. Bayesian analysis of transverse signal decay with application to human brain. Magnetic Resonance in Medicine. 2015; 74(3):785–802. [PubMed: 25242062]
25. Bouhrara M, Spencer RG. Improved determination of the myelin water fraction in human brain using magnetic resonance imaging through Bayesian analysis of mcDESPOT. NeuroImage. 2016; 127:456–71. [PubMed: 26499810]

26. Dean DC 3rd, O'Muircheartaigh J, Dirks H, Waskiewicz N, Lehman K, Walker L, et al. Estimating the age of healthy infants from quantitative myelin water fraction maps. Human Brain Mapping. 2015; 36(4):1233–44. [PubMed: 25640476]
27. Deoni SC, Matthews L, Kolind SH. One component? Two components? Three? The effect of including a nonexchanging "free" water component in multicomponent driven equilibrium single pulse observation of T1 and T2. Magnetic resonance in medicine. 2013; 70(1):147–54. [PubMed: 22915316]
28. Deoni SC, Rutt BK, Arun T, Pierpaoli C, Jones DK. Gleaning multicomponent T1 and T2 information from steady-state imaging data. Magnetic Resonance in Medicine. 2008; 60(6):1372–87. [PubMed: 19025904]
29. Hwang D, Kim DH, Du YP. In vivo multi-slice mapping of myelin water content using T2* decay. NeuroImage. 2010; 52(1):198–204. [PubMed: 20398770]
30. Kolind S, Seddigh A, Combes A, Russell-Schulz B, Tam R, Yogendrakumar V, et al. Brain and cord myelin water imaging: a progressive multiple sclerosis biomarker. NeuroImage Clinical. 2015; 9:574–80. [PubMed: 26594633]
31. Laule C, Leung E, Lis DK, Traboulsee AL, Paty DW, MacKay AL, et al. Myelin water imaging in multiple sclerosis: quantitative correlations with histopathology. Multiple Sclerosis (Houndmills, Basingstoke, England). 2006; 12(6):747–53.
32. Lenz C, Klarhofer M, Scheffler K. Feasibility of in vivo myelin water imaging using 3D multigradient-echo pulse sequences. Magnetic Resonance in Medicine. 2012; 68(2):523–8. [PubMed: 22213038]
33. Zhang J, Kolind SH, Laule C, MacKay AL. Comparison of myelin water fraction from multiecho T2 decay curve and steady-state methods. Magnetic Resonance in Medicine. 2015; 73(1):223–32. [PubMed: 24515972]
34. Rioux JA, Levesque IR, Rutt BK. Biexponential longitudinal relaxation in white matter: Characterization and impact on T mapping with IR-FSE and MP2RAGE. Magnetic Resonance in Medicine. 2015
35. Whittall KP, MacKay AL, Graeb DA, Nugent RA, Li DK, Paty DW. In vivo measurement of T2 distributions and water contents in normal human brain. Magnetic Resonance in Medicine. 1997; 37(1):34–43. [PubMed: 8978630]
36. Akhondi-Asl A, Afacan O, Balasubramanian M, Mulkern RV, Warfield SK. Fast myelin water fraction estimation using 2D multislice CPMG. Magnetic Resonance in Medicine. 2015
37. Prasloski T, Rauscher A, MacKay AL, Hodgson M, Vavasour IM, Laule C, et al. Rapid whole cerebrum myelin water imaging using a 3D GRASE sequence. NeuroImage. 2012; 63(1):533–9. [PubMed: 22776448]
38. Prasloski T, Madler B, Xiang QS, MacKay A, Jones C. Applications of stimulated echo correction to multicomponent T2 analysis. Magnetic Resonance in Medicine. 2012; 67(6):1803–14. [PubMed: 22012743]
39. Nguyen TD, Deh K, Monohan E, Pandya S, Spincemaille P, Raj A, et al. Feasibility and reproducibility of whole brain myelin water mapping in 4 minutes using fast acquisition with spiral trajectory and adiabatic T2prep (FAST-T2) at 3T. Magnetic Resonance in Medicine. 2015
40. Oh J, Han ET, Lee MC, Nelson SJ, Pelletier D. Multislice brain myelin water fractions at 3T in multiple sclerosis. Journal of Neuroimaging : Official Journal of the American Society of Neuroimaging. 2007; 17(2):156–63. [PubMed: 17441837]
41. Armspach JP, Gounot D, Rumbach L, Chambron J. In vivo determination of multiexponential T2 relaxation in the brain of patients with multiple sclerosis. Magnetic Resonance Imaging. 1991; 9(1):107–13. [PubMed: 2056848]
42. Vargas WS, Monohan E, Pandya S, Raj A, Vartanian T, Nguyen TD, et al. Measuring longitudinal myelin water fraction in new multiple sclerosis lesions. NeuroImage Clinical. 2015; 9:369–75. [PubMed: 26594620]
43. Baranovicova E, Mlynarik V, Kantorova E, Hnilicova P, Dobrota D. Quantitative evaluation of cerebral white matter in patients with multiple sclerosis using multicomponent T2 mapping. Neurological Research. 2016; 38(5):389–96. [PubMed: 27078709]

44. Deoni SC. Correction of main and transmit magnetic field (B0 and B1) inhomogeneity effects in multicomponent-driven equilibrium single-pulse observation of T1 and T2. Magnetic Resonance in Medicine. 2011; 65(4):1021–35. [PubMed: 21413066]
45. Croteau-Chonka EC, Dean DC 3rd, Remer J, Dirks H, O'Muircheartaigh J, Deoni SC. Examining the relationships between cortical maturation and white matter myelination throughout early childhood. NeuroImage. 2016; 125:413–21. [PubMed: 26499814]
46. Liu F, Block WF, Kijowski R, Samsonov A. Rapid multicomponent relaxometry in steady state with correction of magnetization transfer effects. Magnetic Resonance in Medicine. 2015
47. Bouhrara M, Reiter DA, Celik H, Fishbein KW, Kijowski R, Spencer RG. Analysis of mcDESPOT- and CPMG-derived parameter estimates for two-component nonexchanging systems. Magnetic Resonance in Medicine. 2016; 75(6):2406–2420. [PubMed: 26140371]
48. Lankford CL, Does MD. On the inherent precision of mcDESPOT. Magnetic Resonance in Medicine. 2013; 69(1):127–36. [PubMed: 22411784]
49. Zhang J, Kolind SH, Laule C, MacKay AL. How does magnetization transfer influence mcDESPOT results? Magnetic Resonance in Medicine. 2015; 74(5):1327–35. [PubMed: 25399771]
50. Lankford CL, Dortch RD, Does MD. Fast T2 mapping with multiple echo, caesar cipher acquisition and model-based reconstruction. Magnetic Resonance in Medicine. 2015; 73(3):1065–74. [PubMed: 24753216]
51. Deoni SC, Kolind SH. Investigating the stability of mcDESPOT myelin water fraction values derived using a stochastic region contraction approach. Magnetic Resonance in Medicine. 2015; 73(1):161–9. [PubMed: 24464472]
52. Bouhrara M, Spencer RG. Incorporation of nonzero echo times in the SPGR and bSSFP signal models used in mcDESPOT. Magnetic Resonance in Medicine. 2015; 74(5):1227–35. [PubMed: 26407635]
53. Deoni SC. Transverse relaxation time (T2) mapping in the brain with off-resonance correction using phase-cycled steady-state free precession imaging. Journal of Magnetic Resonance Imaging. 2009; 30(2):411–7. [PubMed: 19629970]
54. Berger MF, Silverman HF. Microphone array optimization by stochastic region contraction. Signal Processing, IEEE Transactions on. 1991; 39(11):2377–86.
55. Oh J, Han ET, Pelletier D, Nelson SJ. Measurement of in vivo multi-component T2 relaxation times for brain tissue using multi-slice T2 prep at 1.5 and 3 T. Magnetic Resonance Imaging. 2006; 24(1):33–43. [PubMed: 16410176]
56. Nam Y, Lee J, Hwang D, Kim DH. Improved estimation of myelin water fraction using complex model fitting. NeuroImage. 2015; 116:214–21. [PubMed: 25858448]
57. van Gelderen P, de Zwart JA, Lee J, Sati P, Reich DS, Duyn JH. Non-exponential T(2)(*) decay in White Matter. Magnetic Resonance in Medicine. 2012; 67(1):110–7. [PubMed: 21630352]
58. Raj A, Pandya S, Shen X, LoCastro E, Nguyen TD, Gauthier SA. Multi-Compartment T2 Relaxometry Using a Spatially Constrained Multi-Gaussian Model. PloS One. 2014; 9(6):e98391. [PubMed: 24896833]
59. Kumar D, Nguyen TD, Gauthier SA, Raj A. Bayesian algorithm using spatial priors for multiexponential T2 relaxometry from multiecho spin echo MRI. Magnetic Resonance in Medicine. 2012; 68(5):1536–43. [PubMed: 22266707]
60. Yoo Y, Prasloski T, Vavasour I, MacKay A, Traboulsee AL, Li DK, et al. Fast computation of myelin maps from MRI T(2) relaxation data using multicore CPU and graphics card parallelization. Journal of Magnetic Resonance Imaging. 2015; 41(3):700–7. [PubMed: 24578324]
61. Björk M, Zachariah D, Kullberg J, Stoica P. A multicomponent T2 relaxometry algorithm for myelin water imaging of the brain. Magnetic Resonance in Medicine. 2016; 75(1):390–402. [PubMed: 25604436]
62. Nam Y, Kim DH, Lee J. Physiological noise compensation in gradient-echo myelin water imaging. NeuroImage. 2015; 120:345–9. [PubMed: 26172308]
63. Lee J, Nam Y, Choi JY, Kim EY, Oh S-H, Kim D-H. Mechanisms of T2* anisotropy and gradient echo myelin water imaging. NMR in Biomedicine. 2016 n/a-n/a.

64. Ganzetti M, Wenderoth N, Mantini D. Whole brain myelin mapping using T1- and T2-weighted MR imaging data. Frontiers in Human Neuroscience. 2014:8. [PubMed: 24478674]

65. Warntjes M, Engström M, Tisell A, Lundberg P. Modelling the presence of myelin and oedema in the brain based on multi-parametric quantitative MRI. Frontiers in Neurology. 2016:7. [PubMed: 26869987]

66. Qian SS, Stow CA, Borsuk ME. On Monte Carlo methods for Bayesian inference. Ecological Modelling. 2003; 159(2–3):269–77.

67. Kolind S, Matthews L, Johansen-Berg H, Leite MI, Williams SC, Deoni S, et al. Myelin water imaging reflects clinical variability in multiple sclerosis. NeuroImage. 2012; 60(1):263–70. [PubMed: 22155325]

68. Ziener CH, Kampf T, Jakob PM, Bauer WR. Diffusion effects on the CPMG relaxation rate in a dipolar field. Journal of Magnetic Resonance (San Diego, Calif : 1997). 2010; 202(1):38–42.

69. Deichmann R, Adolf H, Kuchenbrod E, Noth U, Schwarzbauer C, Haase A. Compensation of diffusion effects in T2 measurements. Magnetic Resonance in Medicine. 1995; 33(1):113–5. [PubMed: 7891524]

70. Carney CE, Wong ST, Patz S. Analytical solution and verification of diffusion effect in SSFP. Magnetic Resonance in Medicine. 1991; 19(2):240–6. [PubMed: 1881310]

71. Le Bihan D, Turner R, MacFall JR. Effects of intravoxel incoherent motions (IVIM) in steady-state free precession (SSFP) imaging: application to molecular diffusion imaging. Magnetic Resonance in Medicine. 1989; 10(3):324–37. [PubMed: 2733589]

72. Myint W, Ishima R. Chemical exchange effects during refocusing pulses in constant-time CPMG relaxation dispersion experiments. Journal of biomolecular NMR. 2009; 45(1–2):207–16. [PubMed: 19618276]

73. Kalantari S, Laule C, Bjarnason TA, Vavasour IM, MacKay AL. Insight into in vivo magnetization exchange in human white matter regions. Magnetic Resonance in Medicine. 2011; 66(4):1142–51. [PubMed: 21381107]

74. Majumdar S, Orphanoudakis SC, Gmitro A, O'Donnell M, Gore JC. Errors in the measurements of T2 using multiple-echo MRI techniques. II. Effects of static field inhomogeneity. Magnetic Resonance in Medicine. 1986; 3(4):562–74. [PubMed: 3747818]

75. Knopp T, Eggers H, Dahnke H, Prestin J, Senegas J. Iterative off-resonance and signal decay estimation and correction for multi-echo MRI. IEEE Transactions on Medical Imaging. 2009; 28(3):394–404. [PubMed: 19244011]

76. Zweckstetter M, Holak TA. An adiabatic multiple spin-echo pulse sequence: removal of systematic errors due to pulse imperfections and off-resonance effects. Journal of Magnetic Resonance (San Diego, Calif : 1997). 1998; 133(1):134–47.

77. Bieri O, Scheffler K. Optimized balanced steady-state free precession magnetization transfer imaging. Magnetic Resonance in Medicine. 2007; 58(3):511–8. [PubMed: 17763346]

78. Weber OM, Speier P, Scheffler K, Bieri O. Assessment of magnetization transfer effects in myocardial tissue using balanced steady-state free precession (bSSFP) cine MRI. Magnetic Resonance in Medicine. 2009; 62(3):699–705. [PubMed: 19572387]

79. Sled JG, Pike GB. Quantitative interpretation of magnetization transfer in spoiled gradient echo MRI sequences. Journal of Magnetic Resonance (San Diego, Calif : 1997). 2000; 145(1):24–36.

80. Allerhand A. Analysis of Carr—Purcell Spin-Echo NMR Experiments on Multiple-Spin Systems. I. The Effect of Homonuclear Coupling. The Journal of Chemical Physics. 1966; 44(1):1–9.

81. Stables LA, Kennan RP, Anderson AW, Gore JC. Density matrix simulations of the effects of J coupling in spin echo and fast spin echo imaging. Journal of Magnetic Resonance (San Diego, Calif : 1997). 1999; 140(2):305–14.

82. Mayer D, Dreher W, Leibfritz D, Spielman DM. RF refocused echoes of J-coupled spin systems: effects on RARE-based spectroscopic imaging. Magnetic Resonance in Medicine. 2007; 57(5): 967–71. [PubMed: 17457878]

83. Santyr GE, Henkelman RM, Bronskill MJ. Variation in measured transverse relaxation in tissue resulting from spin locking with the CPMG sequence. Journal of Magnetic Resonance (1969). 1988; 79(1):28–44.

84. Ulmer JL, Mathews VP, Hamilton CA, Elster AD, Moran PR. Magnetization transfer or spin-lock? An investigation of off-resonance saturation pulse imaging with varying frequency offsets. AJNR American Journal of Neuroradiology. 1996; 17(5):805–19. [PubMed: 8733952]

85. Seland JG, Washburn KE, Anthonsen HW, Krane J. Correlations between diffusion, internal magnetic field gradients, and transverse relaxation in porous systems containing oil and water. Physical Review E, Statistical, Nonlinear, and Soft matter Physics. 2004; 70(5 Pt 1):051305.

86. Washburn KE, Eccles CD, Callaghan PT. The dependence on magnetic field strength of correlated internal gradient relaxation time distributions in heterogeneous materials. Journal of Magnetic Resonance (San Diego, Calif : 1997). 2008; 194(1):33–40.

87. Preibisch C, Deichmann R. Influence of RF spoiling on the stability and accuracy of T1 mapping based on spoiled FLASH with varying flip angles. Magnetic Resonance in Medicine. 2009; 61(1): 125–35. [PubMed: 19097220]

88. Yarnykh VL. Optimal radiofrequency and gradient spoiling for improved accuracy of T1 and B1 measurements using fast steady-state techniques. Magnetic Resonance in Medicine. 2010; 63(6): 1610–26. [PubMed: 20512865]

89. Zheng S, Xia Y. On the measurement of multi-component T2 relaxation in cartilage by MR spectroscopy and imaging. Magnetic Resonance Imaging. 2010; 28(4):537–45. [PubMed: 20061115]

90. Levesque IR, Chia CL, Pike GB. Reproducibility of in vivo magnetic resonance imaging-based measurement of myelin water. Journal of Magnetic Resonance Imaging. 2010; 32(1):60–8. [PubMed: 20578011]

91. Wang N, Xia Y. Experimental issues in the measurement of multi-component relaxation times in articular cartilage by microscopic MRI. Journal of Magnetic Resonance (San Diego, Calif : 1997). 2013; 235:15–25.

92. Bouhrara M, Bonny JM. B(1) mapping with selective pulses. Magnetic Resonance in Medicine. 2012; 68(5):1472–80. [PubMed: 22246956]

93. McPhee KC, Wilman AH. T2 quantification from only proton density and T2-weighted MRI by modelling actual refocusing angles. NeuroImage. 2015; 118:642–50. [PubMed: 26049150]

94. Murase K. Generalized equation for describing the magnetization in spoiled gradient-echo imaging. Magnetic Resonance Imaging. 2011; 29(5):723–30. [PubMed: 21524871]

95. Bieri O, Scheffler K. SSFP signal with finite RF pulses. Magnetic Resonance in Medicine. 2009; 62(5):1232–41. [PubMed: 19780160]

96. Bieri O. An analytical description of balanced steady-state free precession with finite radio-frequency excitation. Magnetic Resonance in Medicine. 2011; 65(2):422–31. [PubMed: 20859995]

97. Boulant N. T1 and T2 effects during radio-frequency pulses in spoiled gradient echo sequences. Journal of Magnetic Resonance (San Diego, Calif : 1997). 2009; 197(2):213–8.

98. Lenz C, Klarhofer M, Scheffler K. Limitations of rapid myelin water quantification using 3D bSSFP. MAGMA (New York, NY). 2010; 23(3):139–51.

99. Hess AT, Robson MD. Hexagonal gradient scheme with RF spoiling improves spoiling performance for high-flip-angle fast gradient echo imaging. Magnetic Resonance in Medicine. 2016

100. Aja-Fernandez S, Vegas-Sanchez-Ferrero G, Tristan-Vega A. Noise estimation in parallel MRI: GRAPPA and SENSE. Magnetic Resonance Imaging. 2014; 32(3):281–90. [PubMed: 24418329]

101. Bar S, Weigel M, von Elverfeldt D, Hennig J, Leupold J. Intrinsic diffusion sensitivity of the balanced steady-state free precession (bSSFP) imaging sequence. NMR in Biomedicine. 2015; 28(11):1383–92. [PubMed: 26346811]

102. Bieri O, Scheffler K. Effect of diffusion in inhomogeneous magnetic fields on balanced steady-state free precession. NMR in Biomedicine. 2007; 20(1):1–10. [PubMed: 16947639]

103. Jeffreys H. An invariant form for the prior probability in estimation problems. Proceedings of the Royal Society of London Series A, Mathematical and Physical Sciences. 1946; 186(1007):453–61.

6. Appendix

6.1. BMC-mcDESPOT Analysis for the estimation of all system parameters

The estimate, $\hat{\lambda_i}$, of a given parameter, λ_i, belonging to the set of unknown parameters $\boldsymbol{\lambda}$ is given by (25):

$$\hat{\lambda}_i = \int \lambda_i \, \mathrm{P}(\lambda_i|\mathbf{S}) \, \mathrm{d}\lambda_i = \int \cdots \int \lambda_i \frac{P(\boldsymbol{\lambda}^*) L(\mathbf{S}|\boldsymbol{\lambda})}{P(\mathbf{S})} \mathrm{d}\boldsymbol{\lambda} \simeq \sum_{m=1}^{M} \lambda_{i,m} \frac{P(\boldsymbol{\lambda}^*_m) \, L(\mathbf{S}|\boldsymbol{\lambda}_m)}{P(\mathbf{S})}. \quad [A.1]$$

Here, P(λ_i|**S**)is the posterior distribution of λ_i given the vector **S** = (**S**$_{SPGR}$ **S**$_{bSSFP_0}$ **S**$_{bSSFP_\pi}$) of measured signals, each of which is itself a vector describing the signal amplitude for each value of FA, m denotes one of a total of M random sets of parameter combinations sampled from a grid defining the range of our Monte Carlo integration, $\boldsymbol{\lambda}^*$ is equivalent to $\boldsymbol{\lambda}$ but excludes the parameter λ_i being estimated and so represents the vector of nuisance parameters in the determination of λ_i, and $P(\boldsymbol{\lambda}^*) = 1/\boldsymbol{\lambda}^*$ is the product of prior distributions for the elements of $\boldsymbol{\lambda}^*$ taken as noninformative Jeffreys priors (25, 103). For example, the prior distribution in the estimation of $T_{1,s}$ is given by: $P(\boldsymbol{\lambda}^*) = 1/\boldsymbol{\lambda}^* = (1/f_s) * (1/T_{2,s}) * (1/T_{2,l}) * (1/T_{1,l})$. This is a widely-used though strictly improper prior. $P(\mathbf{S}) = \int P(\boldsymbol{\lambda}^*) \, L(\mathbf{S}|\boldsymbol{\lambda}) \, \mathrm{d}\boldsymbol{\lambda}$ is a normalization constant. We note that, in our previous paper (25), d$\boldsymbol{\lambda}$ in the definition of $P(\mathbf{S})$ was erroneously written as d$\boldsymbol{\lambda}^*$, although the numerical calculations were performed with the correct expression. Finally, $L(\mathbf{S}|\boldsymbol{\lambda})$ is the marginalized joint likelihood function of **S** given $\boldsymbol{\lambda}$ (25):

$$L(\mathbf{S}|\boldsymbol{\lambda}) \propto \left(\left(\tilde{\mathbf{S}}_{SPGR} - \tilde{\mathbf{M}}_{SPGR} \right) \left(\tilde{\mathbf{S}}_{SPGR} - \tilde{\mathbf{M}}_{SPGR} \right)^T \right)^{-\frac{K}{2}} \left(\left(\tilde{\mathbf{S}}_{bSSFP_0} - \tilde{\mathbf{M}}_{bSSFP_0} \right) \left(\tilde{\mathbf{S}}_{bSSFP_0} - \tilde{\mathbf{M}}_{bSSFP_0} \right)^T \right)^{-\frac{N}{2}} \left(\left(\tilde{\mathbf{S}}_{bSSFP_\pi} - \tilde{\mathbf{M}}_{bSSFP_\pi} \right) \left(\tilde{\mathbf{S}}_{bSSFP_\pi} - \tilde{\mathbf{M}}_{bSSFP_\pi} \right)^T \right)^{-\frac{N}{2}}, \quad [A.2]$$

where $\tilde{\mathbf{S}}$ and $\tilde{\mathbf{M}}$ are respectively the experimental and theoretical signals normalized by their respective mean values calculated over K SPGR or N bSSFP FAs (25). The theoretical SPGR and bSSFP signals are given in the following section. For computational efficiency, the likelihood function given in Eq. A. 2 is first calculated for all random parameter combinations. Then, for each parameter, the likelihood function is combined with the corresponding joint prior to create the joint posterior distribution for each of those random parameter combinations. Finally, the parameter estimate is obtained based on the first moment of the joint posterior distribution after marginalization over nuisance parameters.

6.2. SPGR and bSSFP signal models

Neglecting exchange between components, the two-component SPGR signal is given by (52)

$$M^{k}_{SPGR}=M^{0}_{SPGR}\sin(\alpha_k)\left(f_s\frac{E^{\dagger}_{2,s}\left(1-E_{1,s}\right)}{1-E_{1,s}\cos(\alpha_k)}+(1-f_s)\frac{E^{\dagger}_{2,l}\left(1-E_{1,l}\right)}{1-E_{1,l}\cos(\alpha_k)}\right), \quad [1]$$

where s and l respectively denote the short- and long- T_2 components, f_s is the fraction of the short T_2 component, M^{0}_{SPGR} represents the signal amplitude at echo time TE = 0 and incorporates proton density, T_2' and machine factors (47, 52), and α_k is the k^{th} excitation FA out of a total of K FAs. We also define $E^{\dagger}_{2,j}=exp\left(-\mathrm{TE}_{SPGR}/T_{2,j}\right)$ and $E_{1,j}=exp(-\mathrm{TR}_{SPGR}/T_{1,j})$, where $T_{1,j}$ is the spin-lattice and $T_{2,j}$ is the spin-spin relaxation time of the j^{th} component.

Similarly, the two-component bSSFP signal in the absence of exchange between components is given by (52)

$$M^{n}_{bSSFP}=\left|M^{0}_{bSSFP}\left(f_s\left(M^{n}_{a,s}+iM^{n}_{b,s}\right)+(1-f_s)\left(M^{n}_{a,l}+iM^{n}_{b,l}\right)\right)\right|, \quad [2]$$

where

$$M^{n}_{a,j}=\frac{\sqrt{E_{2,j}}\left(1-E_{1,j}\right)\sin(\beta_n)\sin\varphi}{\left(1-E_{1,\mathrm{j}}\cos(\beta_n)\right)\left(1-E_{2,\mathrm{j}}\cos\varphi\right)-E_{2,j}\left(E_{1,j}-\cos(\beta_n)\right)\left(E_{2,j}-\cos\varphi\right)}$$

and

$$M^{n}_{b,j}=\frac{\sqrt{E_{2,j}}\left(1-E_{1,j}\right)\left(\cos\varphi-E_{2,j}\right)\sin(\beta_n)}{\left(1-E_{1,\mathrm{j}}\cos(\beta_n)\right)\left(1-E_{2,\mathrm{j}}\cos\varphi\right)-E_{2,j}\left(E_{1,j}-\cos(\beta_n)\right)\left(E_{2,j}-\cos\varphi\right)}.$$

where M^{0}_{bSSFP} represents the bSSFP signal amplitude at echo time TE = 0 and incorporates proton density and machine factors, β_n is the n^{th} excitation FA out of a total of N FAs, and $\varphi = 2\pi\cdot\Delta\omega\cdot\mathrm{TR}_{bSSFP}+\vartheta$, with $\Delta\omega$ the off-resonance frequency of proton pools with the assumption that both proton pools exhibit the same chemical shift, and ϑ the phase increment of the applied RF pulse. Finally, $E_{1,j}=exp(-\mathrm{TR}_{bSSFP}/\mathrm{T}_{1,j})$ and $E_{2,j}=exp(-\mathrm{TR}_{bSSFP}/T_{2,j})$.

Highlights

- We extend Bayesian Monte Carlo (BMC) analysis of the two-component mcDESPOT signal model to simultaneous estimation of myelin water fraction (MWF) and relaxation times.
- Simulations and *in-vivo* studies indicate the superiority of BMC-mcDESPOT as compared to the conventional approach based on nonlinear least squares analysis.
- We demonstrate that use of BMC-mcDESPOT permits accurate high-resolution mapping of MWF and relaxation times within a clinically realistic acquisition time.

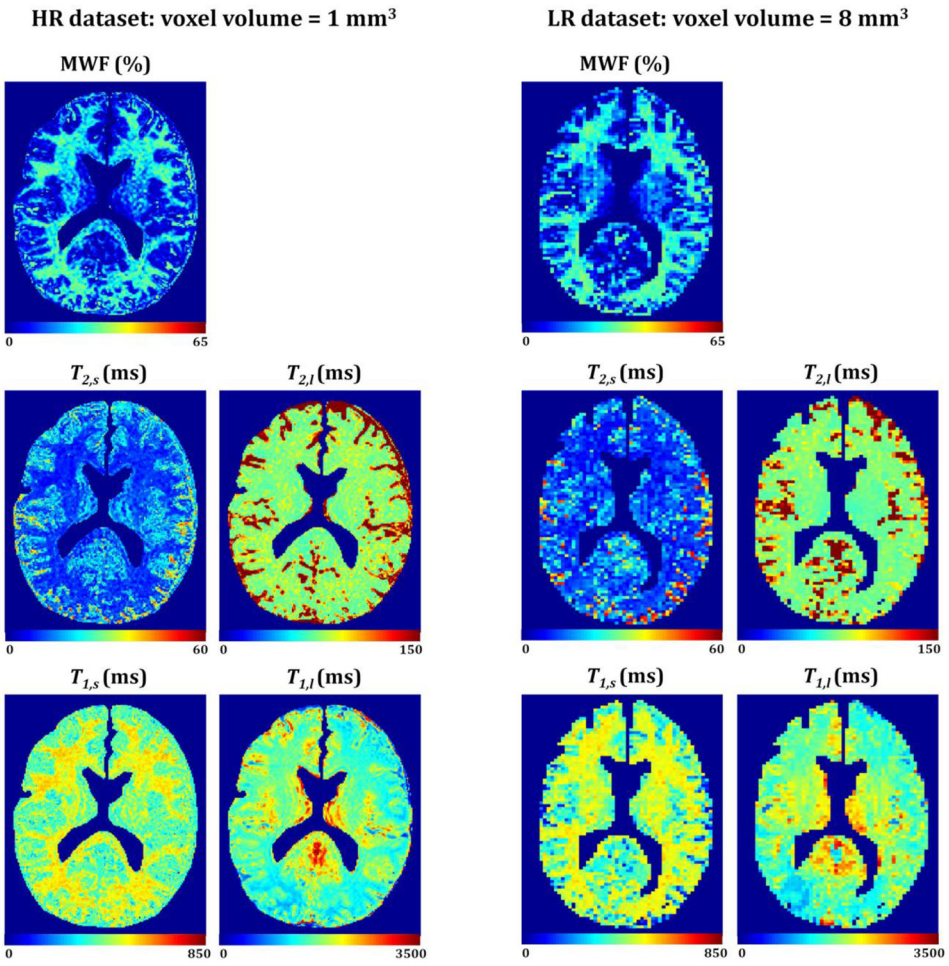

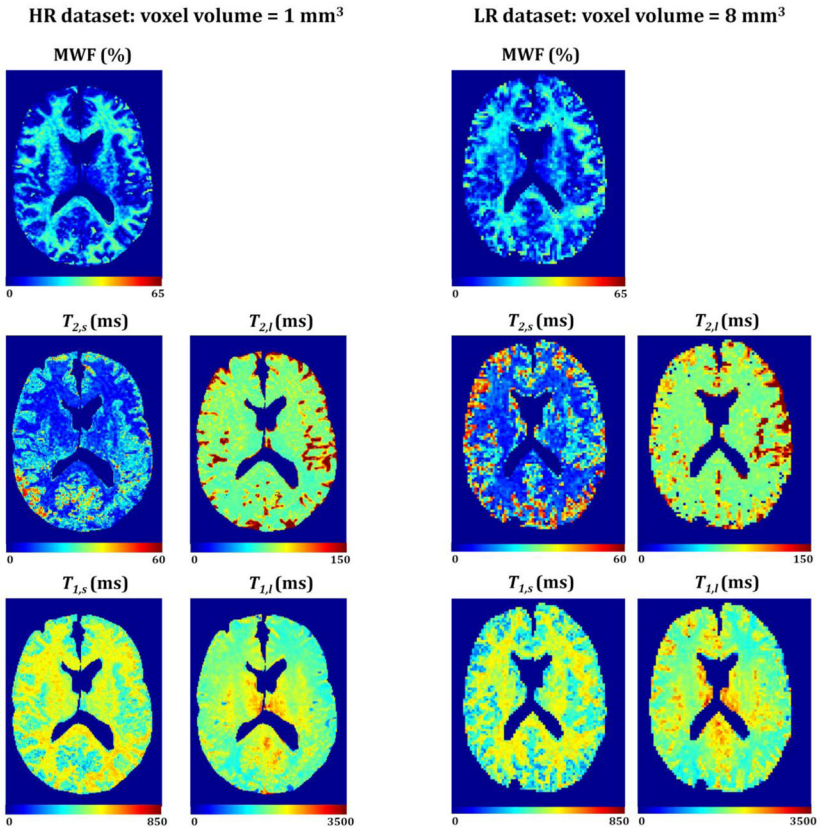

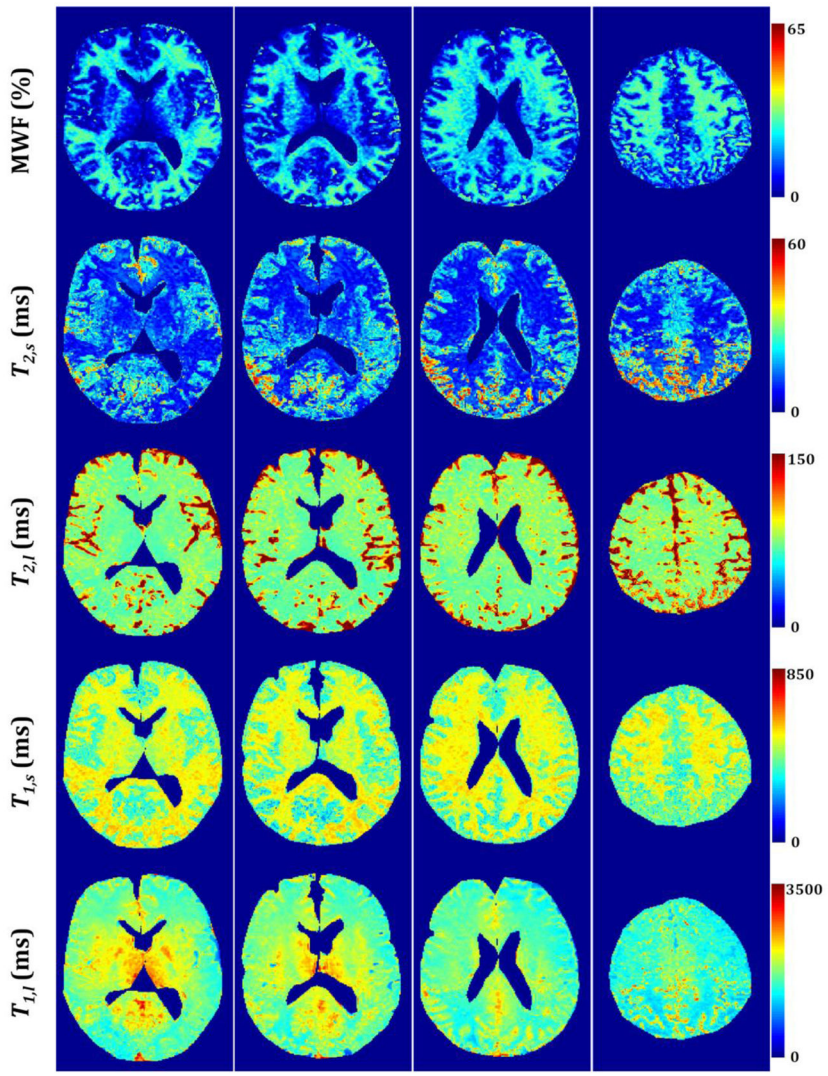

Figure 1.

Figure 1a. Representative MWF, $T_{2,s}$, $T_{2,l}$, $T_{1,s}$, and $T_{1,l}$ maps calculated for Volunteer #1 (Table 1) using BMC-mcDESPOT. Results are presented for both high-resolution (HR) and low-resolution (LR) datasets. The HR maps allows greater depiction of anatomical detail and regional patterns as compared to the LR maps. Note that the displayed color scales are different from the boundary limits of the parameter space used in the fitting process for improved visualization. **1b.** Representative MWF, $T_{2,s}$, $T_{2,l}$, $T_{1,s}$, and $T_{1,l}$ maps calculated for Volunteer #3 (HR, left panels) or Volunteer #4 (LR, right panels) (Table 1) using BMC-mcDESPOT. The HR maps allows greater depiction of anatomic detail and regional patterns as compared to the LR maps. Note that the displayed color scales are different from the boundary limits of the parameter space used in the fitting process. **1c.** High-resolution MWF, $T_{2,s}$, $T_{2,l}$, $T_{1,s}$, and $T_{1,l}$ maps calculated from brain images of Volunteer #3 (Table 1) using BMC-mcDESPOT. Results are presented for four different slices. Note that the displayed color scales are different from the boundary limits of the parameter space used in the fitting process.

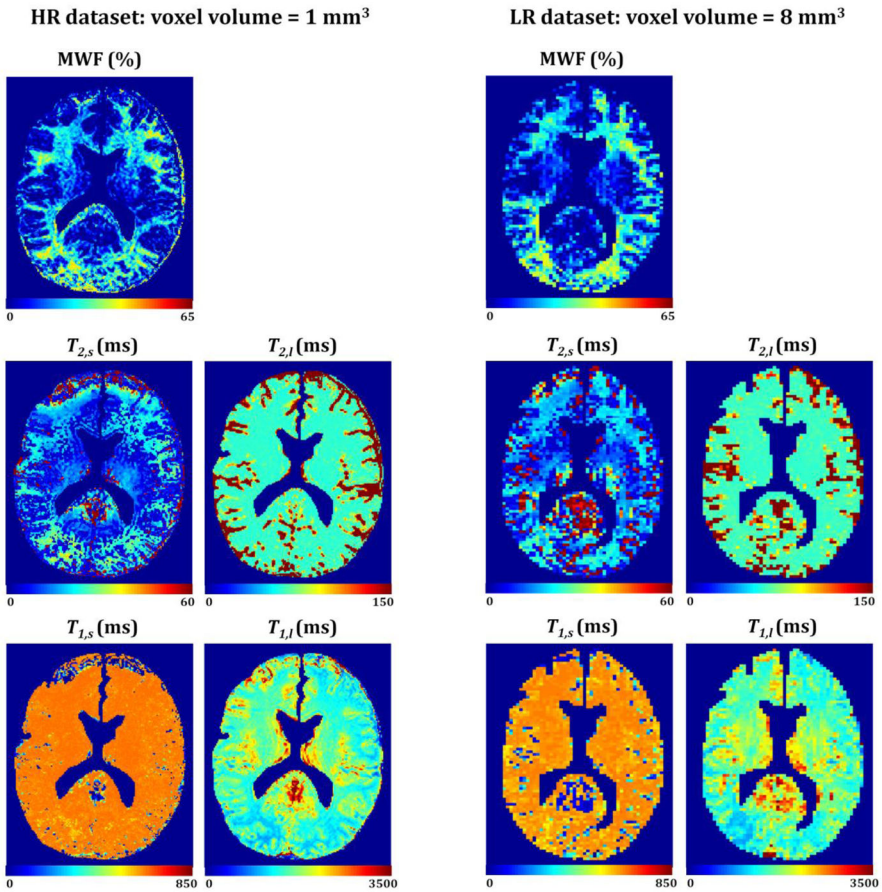

Figure 2.

Representative MWF, $T_{2,s}$, $T_{2,l}$, $T_{1,s}$, and $T_{1,l}$ maps calculated for Volunteer #1 using SRC. Results are presented for both HR and LR datasets. Note that the displayed color scales are different from the boundary limits of the parameter space used in the fitting process.

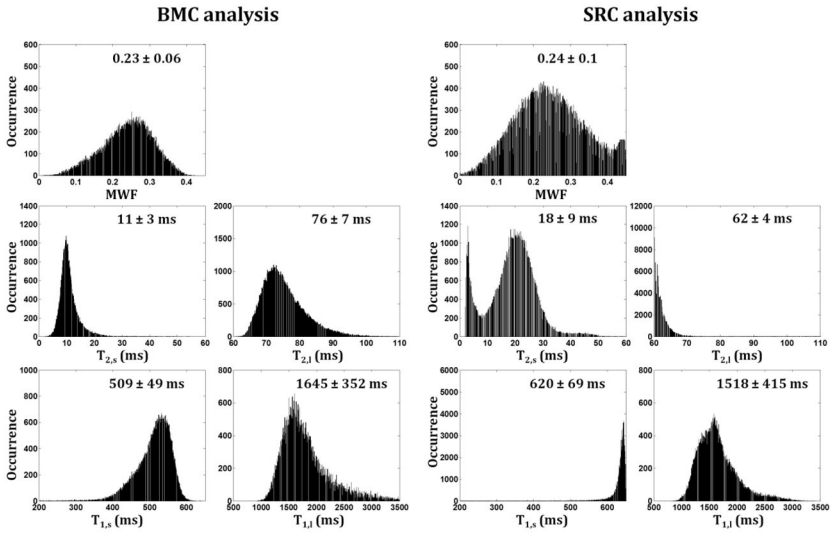

Figure 3.

Representative histograms of MWF, $T_{2,s}$, $T_{2,l}$, $T_{1,s}$ and $T_{1,l}$ obtained using BMC or SRC analysis from white matter regions within the HR parameter maps calculated for Volunteer #1. The mean and standard deviation values are as indicated, with BMC generally outperforming SRC. Unlike BMC, SRC resulted in a clustering of $T_{2,l}$ and $T_{1,s}$ estimates towards the lower and upper search space limits, respectively. These results indicate the superior overall performance of BMC as compared to SRC.

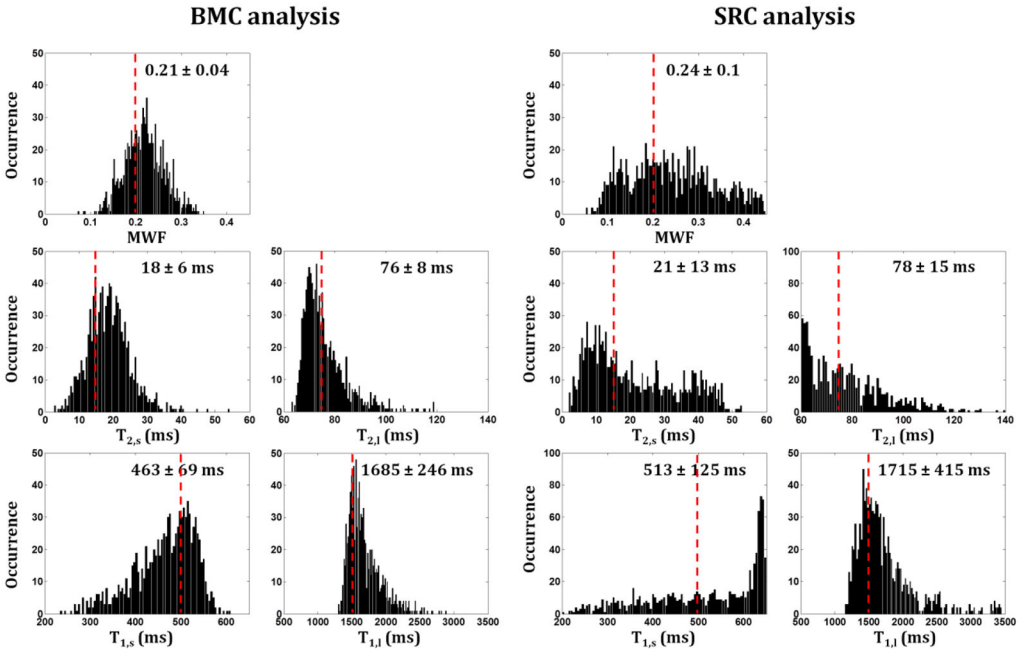

Figure 4.

Histograms of MWF, $T_{2,s}$, $T_{2,l}$, $T_{1,s}$ and $T_{1,l}$ obtained using BMC or SRC analysis over 1001 noise realizations using numerical simulations. Vertical red dashed lines indicate true input parameter values: $f_s = 0.2$, $T_{2,s} = 15$ ms, $T_{2,l} = 75$ ms, $T_{1,s} = 500$ ms and $T_{1,l} = 1500$ ms. The mean and standard deviations are as indicated. Note that using SRC, $T_{2,l}$ estimates were clustered towards the lower search space limit while $T_{1,s}$ estimates were clustered towards the upper search space limit. In contrast, BMC parameter estimates were distributed around the true input values and avoided search space boundaries.

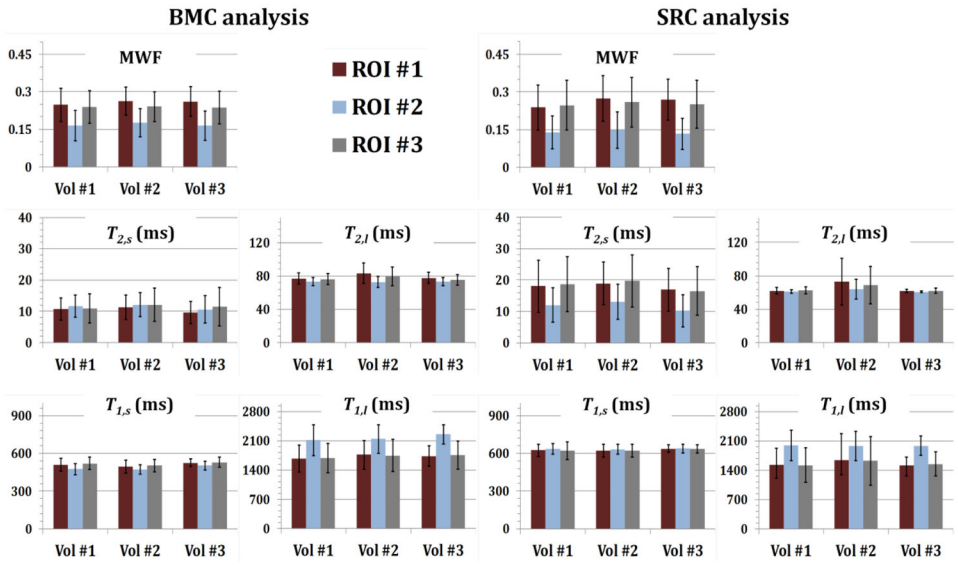

Figure 5.

Means and standard deviations of estimates of MWF, $T_{2,s}$, $T_{2,l}$, $T_{1,s}$ and $T_{1,l}$ calculated from the HR datasets acquired from the brains of three volunteers (Vol) (Table 1). For each HR dataset, results were obtained in three different regions of interest (ROIs) using BMC or SRC analysis. ROI #1 lay within the frontal lobes, ROI #2 lay within the regions surrounded by the insular lobes, internal capsules, thalamus and putamen, and ROI #3 incorporated all WM regions.

Table 1

In-vivo acquisition parameters

Volunteers	Acquisition parameters	
	Low-resolution (LR) protocol	**High-resolution (HR) protocol**
Volunteer #1 Healthy 23 year-old male	3D SPGR: α_{SPGR} = [2 4 6 8 10 12 14 16 18 20]°, TE_{SPGR} = 1.2 ms, TR_{SPGR} = 6.5 ms. 3D bSSFP: β_{bSSFP} = [2 6 14 22 30 38 46 54 62 70]°, TE_{bSSFP} = 3.2 ms and TR_{bSSFP} = 6.5 ms.	3D SPGR: α_{SPGR} = [2 4 6 8 10 12 14 16 18 20]°, TE_{SPGR} = 1.2 ms, TR_{SPGR} = 6.5 ms. 3D bSSFP: β_{bSSFP} = [2 6 14 22 30 38 46 54 62 70]°, TE_{bSSFP} = 3.2 ms and TR_{bSSFP} = 6.5 ms.
Volunteer #2 Healthy 22 year-old male	FoV = 230 x 180 x 130 mm^3, matrix size = 116 x 90 x 65, acquisition voxel size ≃ 2 mm x 2 mm x 2 mm, total acquisition time ≃ 10 min.	FoV = 230 x 180 x 130 mm^3, matrix size = 153 x 120 x 86, acquisition voxel size ≃ 1.5 mm x 1.5 mm x 1.5 mm, total acquisition time ≃ 17 min.
Volunteer #3 Healthy 29 year-old male	-	3D SPGR: α_{SPGR} = [2 4 6 8 10 12 14 16 18]°, TE_{SPGR} = 0.83 ms, TR_{SPGR} = 6 ms. 3D bSSFP: β_{bSSFP} = [2 4 7 11 16 24 32 40 50]°, TE_{bSSFP} = 2.8 ms and TR_{bSSFP} = 5.8 ms. FoV = 230 x 190 x 140 mm^3, matrix size = 154 x 127 x 94, acquisition voxel size ≃ 1.5 mm x 1.5 mm x 1.5 mm, total acquisition time ≃ 15 min.
Volunteer #4 Healthy 22 year-old male	3D SPGR: α_{SPGR} = [2 4 6 8 10 12 14 16 18 20]°, TE_{SPGR} = 0.83 ms, TR_{SPGR} = 6 ms. 3D bSSFP: β_{bSSFP} = [2 6 14 22 30 38 46 54 62 70]°, TE_{bSSFP} = 2.8 ms and TR_{bSSFP} = 5.8 ms. FoV = 200 x 216 x 140 mm^3, matrix size = 100 x 108 x 70, acquisition voxel size ≃ 2 mm x 2 mm x 2 mm, total acquisition time ≃ 11 min.	-

*FoV: Field of view. The bSSFP images were acquired twice, once with *RF* phase increment, θ_{RF}, of 0 ($bSSFP_0$) and once with θ_{RF} of π ($bSSFP_\pi$). All images were acquired with SENSE factor = 2. LR images were reconstructed to voxel volume = 8 mm^3 while HR images were reconstructed to voxel volume = 1 mm^3.